

THE INFLUENCE OF FAULTING STYLE ON THE SIZE-DISTRIBUTION OF GLOBAL EARTHQUAKES

A. Petruccelli ^{a,b}, D. Schorlemmer ^c, T. Tormann ^b, A. P. Rinaldi ^b, S. Wiemer ^b, P. Gasperini ^a, G.
Vannucci ^d

^a Dipartimento di Fisica e Astronomia, University of Bologna, Italy.

^b Swiss Seismological Service, ETH Zurich, Switzerland.

^c Helmholtz Centre Potsdam, GFZ Potsdam, Germany.

^d Istituto Nazionale di Geofisica e Vulcanologia, Bologna, Italy.

A. Petruccelli: Antonio Petruccelli (antonio.petruccelli4@unibo.it) ¹

D. Schorlemmer: Danijel Schorlemmer (danijel.schorlemmer@gfz-potsdam.de)

T. Tormann: Thessa Tormann (thessa@sed.ethz.ch) ²

A. P. Rinaldi: Antonio Pio Rinaldi (antoniopio.rinaldi@sed.ethz.ch)

S. Wiemer: Stefan Wiemer (stefan.wiemer@sed.ethz.ch)

P. Gasperini: Paolo Gasperini (paolo.gasperini@unibo.it)

G. Vannucci: Gianfranco Vannucci (gianfranco.vannucci@ingv.it)

¹ **Corresponding author**, now at Swiss Seismological Service SED, ETH Zürich, Switzerland:
antonio.petruccelli@sed.ethz.ch

² Now at PartnerRe, Zürich, Switzerland

Abstract: We derive a unifying formulation, reliable at all scales, linking Anderson's faulting theory with the earthquake-size distribution, whose exponent is known as b -value. Anderson's theory, introduced in 1905, relates fault orientation and stress conditions. Independently, laboratory measurements on acoustic emissions have established that the applied differential stress controls their b -value. Our global survey reveals that observed spatial variations of b are controlled by different stress regimes, generally being lower in compressional (subduction trenches and continental collisional systems) and higher in extensional regimes (oceanic ridges), confirming previous observations on the dependence of b -value on the angle of rake of focal mechanisms. Using a new plunge/dip-angles-based b -value analysis, we also identify further systematic influences of faulting geometry: steep normal faults (also typical of oldest subduction zones) have the highest proportion of smaller events, while low-angle thrust faults (typical of youngest subduction zones) experiencing proportionally larger, more hazardous, events, differently from what expected by allowing only a rake angle dependency. To date, however, no physical model has ever been proposed to explain how earthquakes size-distribution, differential stress and faulting styles relate each other. We here accomplish the task, by proposing and analytically deriving a unifying theory for describing how fault orientation and differential stresses determine b -value. By applying a Mohr-Coulomb failure criterion in a simple dip-slip faulting configuration and by assuming inverse linearity between b -value and differential stress. Our empirical theory contemporary confirms that b decays linearly with increasing differential stress but predicting a different dip-dependent modulation according to the tectonic environment, opening up new ways to assess the seismic hazard of a region.

Keywords: Statistical seismology, Earthquake-size distribution, Faulting styles, Anderson's theory of faulting, Mohr-Coulomb failure criterion

1. Introduction

One of the ongoing debates in seismology concerns the understanding of the physical implications of the earthquake-size distribution, its potential variations on different scales and its use in earthquake hazard assessment and forecasting. Empirically, the behavior of the number of detected earthquakes $N(M)$ at a magnitude M is generally well expressed by the Gutenberg-Richter (GR³) (Gutenberg and Richter, 1944) relation

$$\log N(M) = a - bM \quad (1)$$

In this GR relation, the b -value (commonly 1) quantifies the relative proportion of larger to smaller earthquakes: the lower the b -value, the higher the relative frequency of large magnitude events and, in general, the higher the seismic hazard. The large amount of publications on GR b -values reflects the importance of a proper understanding of such parameter.

The stress distribution in the crust is a critical parameter for understanding earthquake nucleation, but due to the sparsity of in-situ measurements, stressing conditions on faults are probably the key unknown for advancing earthquake forecasting. Laboratory measurements conducted repeatedly since the 1960s (Amitrano, 2003; Goebel et al., 2013; Scholz, 1968) have established that the differential stress (i.e. the difference between the maximum, σ_1 , and minimum, σ_3 , principal stress in the stress tensor) applied to a rock sample determines the b -value of acoustic emissions: the higher the applied differential stress, the lower the b -value. On the other side, other factors such as confining and pore fluid pressure (and hence mean effective stress) (Sammonds et al., 1992), material heterogeneity (Mogi, 1962), which itself controls fracture toughness, might play a role in causing b -

³ Abbreviations used along the manuscript: b : b -value; CMT: centroid moment tensor; FM: focal mechanism; FS: faulting style; GR: Gutenberg and Richter law; NR: normal faulting mechanisms; S2005: Schorlemmer et al. (2005); SHA: seismic hazard assessment; SS: strike-slip mechanisms; TH: thrust faulting mechanisms.

value to vary. However, a range of observations are in good agreement with these laboratory results: asperities, locked patches of faults are, by definition, areas of high differential stress, and many observational studies have shown them to exhibit low b -values (Cao and Gao, 2002; Ghosh et al., 2008; Schorlemmer and Wiemer, 2005; Tormann et al., 2015, 2014, 2012). Weak zones, by contrast, such as creeping sections of faults, mid-ocean ridges and volcanic regions typically have high b -values (Farrell et al., 2009; Kagan, 1997; Okal and Romanowicz, 1994; Roberts et al., 2015; Schorlemmer et al., 2004; Tormann et al., 2014). Parallely, another interpretation (Amitrano, 2012), based on the theory of critical phase transition, explains the apparent decrease in b -value as due to the truncation of the power law by an exponential, whose characteristic size increases as the rupture approaches.

Anderson's theory of faulting (Anderson, 1905) defines three possible styles, depending on the orientation of the three principal stresses. For a faulting style, the differential stress required for reactivation is strictly linked to frictional properties and fault orientation. In case of reactivation, for optimally-oriented faults, the expected dip varies with the friction coefficient μ , causing then different amounts of stress levels on the fault planes. For a coefficient of about 0.6, the dip angle is $\sim 30^\circ$ and $\sim 60^\circ$ for compressive and extensive faults, respectively. Intermediate stress conditions characterize instead $\sim 90^\circ$ dipping transcurrent faults. Indeed, a systematic dependence of b -values on faulting style – via rake angle λ of FM - for global and regional datasets has been proposed (Gulia and Wiemer, 2010; A. Petruccelli et al., 2018; Schorlemmer et al., 2005; Yang et al., 2012). Extensional regimes dominated by normal faulting (NR, $\lambda = -90^\circ$) are characterized by the highest b -values (~ 1.1 - 1.2), whereas regimes dominated by thrust faulting (TH, $\lambda = 90^\circ$) are subject to the highest differential stress and have low b -values (~ 0.7 - 0.9), and strike-slip faults (SS, $\lambda = 0, \pm 180^\circ$) come in the middle (~ 1). For subduction zones, b -values reportedly depend on local tectonic properties, such as the age of the subducting plate or slab buoyancy (Nishikawa and Ide, 2014).

85 So far, however, there has been no quantitative comparison and model that unifies Anderson's
 86 faulting theory, differential-stress dependency and earthquake-size distribution. To develop such a
 87 framework, we conducted a global earthquakes-size distribution survey and tested if the spatial
 88 patterns of b -values reflect major global seismotectonic structures, as predicted by faulting theory.
 89 We then developed a new analytic approach linking b -values to faulting geometry, using a plunge-
 90 based ternary diagram (Frohlich, 2001; Frohlich and Apperson, 1992). Finally, we combined those
 91 analyses of b with fault modelling and derive a relationship linking b -values with differential stress
 92 to be applied for fault modelling.

93 **2. Empirical model: theory and calculation**

94 We developed a model to explain the observed variations of b -values with plunge δ_T . Anderson's
 95 faulting theory (Anderson, 1905) describes the stress conditions needed to activate a fault in a given
 96 orientation and given the frictional properties of the rock. For pure dip-slip faults, the difference
 97 between maximum and minimum tectonic stress ($\Delta\sigma_{hV} = \sigma_h - \sigma_v$), corresponds in absolute values to
 98 the differential stress ($\Delta\sigma = \sigma_1 - \sigma_3$), difference between maximum and minimum principal stress.
 99 Applying the Mohr-Coulomb failure criterion (Coulomb, 1776), given a friction coefficient μ , the
 100 differential stress required to reactivate a dip-slip fault with dip β can be expressed as a function of
 101 δ_T as (see Appendix A for details and Fig. S1):

$$102 \quad \Delta\sigma(\delta_T|\mu) = \frac{C+2\mu(\rho gz-p)}{\pm \sin 2\beta(\delta_T)-\mu[1-\cos 2\beta(\delta_T)]} \quad (2)$$

103 where the plus sign (+) applies to TH events and the minus sign (-) applies to NR events, $\rho gz - p$ is
 104 lithostatic stress (ρ is the assumed crustal density, g is gravity and z is depth) corrected for hydrostatic
 105 pressure p , and C is material cohesion. We assume a lithostatic stress of 83 MPa (with a density of
 106 2,700 kg/m³ and a depth of 5,000 m with hydrostatic pressure), a range of 0.6 – 0.8 for friction
 107 coefficient and a cohesionless fault (i.e. $C = 0$ MPa). We assume a single, uniform, reference depth
 108 in our model, as depth behaves as a scaling factor in our relationship, without playing a role in

differential stress modulation with δ_T , as well as assuming a uniform mean effective stress. On the other side, depth information on global scale is poorly constrained (Ekström et al., 2012).

Although the stress levels in the Earth crust acting on faults are generally not known, these differential stresses inferred from equation (2) can be actually compared with b -values. As general trend, b -value and inferred differential stress seems to have an inverse proportionality, as already proposed by (Scholz, 2015), having as parameters a reference value b_r (1.23) and a global stress-gradient k (0.0012 MPa⁻¹) computed from a linear regression procedure over depth-data (Spada et al., 2013) coming from different regions of the world. The general, linear relation is obtained by assuming a global friction coefficient of 0.75 and different stress-gradients according to the local dominant tectonic regime: for compressional regions dominated by TH a vertical gradient of differential stress of 45 MPa/km, for extensional regions dominated by NR a gradient of 11.25 MPa/km and for SS regions a gradient of 20 MPa/km.

Actually, according to the region considered (Scholz, 2002), the stress-gradient (as well as the reference b_r) can be a constant k_{FS} depending on the faulting style (FS), so that:

$$b(\Delta\sigma) = b_{r,FS} - k_{FS}\Delta\sigma \quad (3)$$

This suggest that indeed b -values of global earthquakes are determined by the respective differential stress levels set by the faulting regime. We can then generalize the relation proposed by (Scholz, 2015) for dip-slip regimes combining equations 2 and 3 as:

$$b(\delta_T|b_{FS}, k_{FS}, \mu) = b_{FS} \mp k_{FS} \frac{[C+2\mu(\rho g z - p)]}{\sin 2\beta(\delta_T) \mp \mu[1 - \cos 2\beta(\delta_T)]} \quad (4)$$

with the upper sign referring to TH and lower sign for NR fault zones, while b_{FS} and k_{FS} are faulting-style dependent constants of the system. As global seismicity is dominated by subduction events (mostly TH), we use the overall b_r and k values of Scholz (Scholz, 2015) in Equation (4) for TH

regime (1.23 and 0.0012 MPa⁻¹), while we need to estimate some new ones for the NR regime (0.28 and 0.013 MPa⁻¹).

The unifying model (4) combine the empirically-observed inverse proportionality between b and differential stress $\Delta\sigma$ which in turn is modulated by a frictional term that includes variations in dip angle β . Equation (4) is only valid in a dip-slip configuration (NR-TH, $\lambda = \pm 90^\circ$), where one of the principal axes is assumed to be vertical (σ_1 or σ_3 respectively) and the intermediate one (σ_2) is always horizontal (see Fig. S1).

2. Global survey of b -value (and M_c)

If differential stresses impact b -values not only at laboratory scale but also in nature, we must expect b -values to vary systematically between different tectonic provinces around the globe. To test this hypothesis, we conducted the most comprehensive global survey of b -values to date, based on the Global CMT (Dziewonski et al., 1981; Ekström et al., 2012) catalogue covering the period 1 January 1980 to 30 September 2016 (Fig. 1). We limited our analysis to earthquakes with a hypocentral depth of 0–50 km (Schorlemmer et al., 2005) and used moment magnitudes M_w binned to $\Delta M = 0.1$. The GCMT catalogue provides strike, dip, and rake values for both nodal planes (Ekström et al., 2012), referring to the first plane as plane 1 and to the second as plane 2.

For each earthquake, we estimated the local b -value (Fig. 1) and the local M_c (Fig. 2A) from the closest seismicity and plotted this value at the epicenter (Figs. 1, 2). Spatial b and distributions are often computed by selecting events within sampling volumes on regular grids (Wiemer and Wyss, 2000). However, in view of the non-uniformity of global earthquake density, we adopted a slightly different approach, taking the epicenters of all earthquakes in the top 50 km as nodes. Around each of these nodes, we selected all earthquakes within cylinders of different radii (ranging from 200 km to 1,500 km, step width 100 km) down to a depth of 50 km (Fig. 2B). To ensure reliable parameter

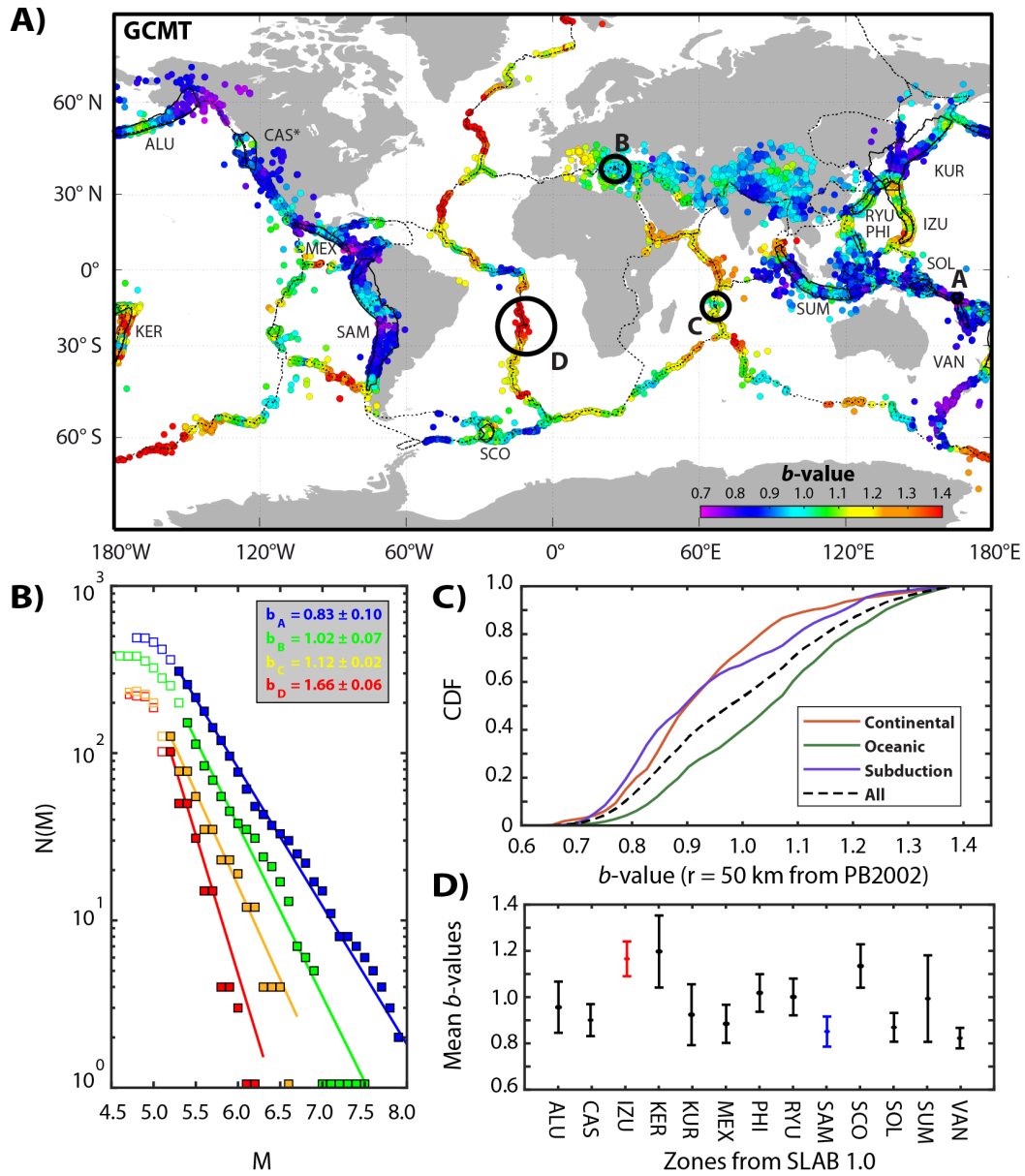
155 estimates, we considered only those cylinders containing a minimum number of 200 events for M_c
156 estimations and more than 100 events above the completeness magnitude for the subsequent b -value
157 estimation. To reach the best possible spatial resolution, we used the smallest of the above cylinders
158 exceeding the required event numbers. We estimated M_c using the “Maximum-Curvature” method
159 (adding 0.2 magnitude units to be conservative) (Wiemer and Wyss, 2002; Woessner and Wiemer,
160 2005) and computed b -values using the standard maximum-likelihood method (Aki, 1965). When
161 assessing standard deviation, computations were bootstrapped 100 times.

162

163 We found statistically significant and highly systematic variations of b -values (Fig. 1A), consistent
164 with the hypothesis and in line with previous works (Kagan, 1997; Nishikawa and Ide, 2014). The
165 three major tectonic categories on Earth are distinctly different (Fig. 1A, B). We found the highest b -
166 values along mid-ocean ridges, the lowest b -values in subduction zones and intermediate b -values in
167 continental zones typically characterized by a mixture of faulting styles. When using, for example,
168 Utsu's test (Utsu, 1966), the populations distinctly differ at significance levels below 0.01 (see Table
169 1). Figure 1B shows earthquake-size distributions in four selected locations. We also check that the
170 observed values are well described by a power-law behavior (see Appendix): we perform a goodness-
171 of-fit test of A, B, C, D distributions in Fig. 1B with a GR model (Aki, 1965), getting for all of them
172 percentage of fit greater or equal about 90%.

173 To test whether the tectonic regime is a statistically significant predictor of b -values, we first derived
174 the distribution of b -values separately for each regime, following a previously published classification
175 schema (Bird, 2003). The resulting distributions (colored lines in Fig. 1C), including the global one
176 (black), are not normally distributed, which we confirmed using a Kolmogorov-Smirnov test (see
177 Table 2). We then applied the non-parametric Wilcoxon signed rank test to decide whether the
178 populations had been sampled from continuous distributions with equal medians (at 5% significance
179 level, see Table 2). We establish that the subduction earthquake-size distribution (blue) is statistically

180 significantly different from the oceanic distribution (green), which in turn differed from the
181 continental distribution (red), establishing that tectonic regime is indeed a predictor of b -value.
182 Subduction zones, however, vary greatly in their structure and characteristics. A first-order
183 classification (Uyeda, 1982; Uyeda and Kanamori, 1979) distinguishes between Chilean-type
184 subduction (fast-moving, young subducting lithosphere with strong compression along strongly
185 coupled interfaces) and Mariana-type subduction (slow-moving, old subducting lithosphere
186 accompanied by extensional roll-back mechanisms and back-arc spreading, but not associated with
187 major earthquakes due to low coupling). We statistically found distinctive global b -values for these
188 specific zones (Fig. 1D): Chilean-type subduction zone tending to have low b -values, and Mariana-
189 type subduction zone higher ones, in agreement with the differential-stress b -value hypothesis (see
190 Fig. S2 and Supplementary Material for further details). However, given that subduction zones can
191 also slip aseismically, there might exist some differences in the seismic-coupling convergence rate
192 relation (Stein and Okal, 2007) for different subduction zones.



193

194 **Figure 1.** A) Map of b -values for the Global CMT (1980-2016) catalogue. Dotted black line: global plate boundary model
 195 PB2002 (Bird, 2003), solid black line: subduction zones according to the SLAB 1.0 model (Hayes et al., 2012) (for
 196 underlying R and M_c maps see Fig. 2). B) Earthquake-size distributions corresponding to points A ($R = 200$ km, $M_c = 5.3$,
 197 perc. fit = 96.1776 %), B ($R = 500$ km, $M_c = 5.4$, perc. fit = 89.1967 %), C ($R = 600$ km, $M_c = 5.2$, perc. fit = 92.7667 %),
 198 and D ($R = 1200$ km, $M_c = 5.2$, perc. fit = 93.0818 %) of a). C) Cumulative density functions (CDFs) of b -values of a)
 199 sampled, moving along the PB2002, within a radius of 50 km. D) Mean b -values for SLAB 1.0 subduction zones, error
 200 bars: standard deviation, red: Mariana zone (high b -values), blue: Chilean zone (low b -values).

Number of events	<i>b</i> -value	Points	A	B	C	D
309	0.83 ± 0.10	A (subduction)	1	0.192	0.02	<i>0</i>
152	1.02 ± 0.07	B (continent)	0.192	1	0.586	0.004
126	1.12 ± 0.02	C (ocean)	0.02	0.586	1	0.015
102	1.66 ± 0.06	D (ocean)	<i>0</i>	0.004	0.015	1

201 **Table 1:** Utsu test P_b , where P_b is the probability of the b -values for A, B, C and D columns in Figures 1A, B (second
202 column) being equal. Bold italic means 5% significance of the null hypothesis and bold indicates 1% significance for the
203 null hypothesis respectively (“significantly” and “high significantly” different b -values). The first column contains the
204 number of complete events used to estimate b -values. P_b of 1 denotes a consistency check while 0 indicated a value lower
205 than 0.01.

Wilcoxon test				Kolmogorov-Smirnov test
PDF	Continents	Oceanic	Subduction	
Continents	1	0	0.06	0
Oceanic	0	1	0	0
Subduction	0.06	0	1	0

206 **Table 2:** Wilcoxon and Kolmogorov-Smirnov tests (last column) for the PDFs of Figure 1C (5% significance level). The
207 Wilcoxon test computes the probability of being wrong in rejecting the null hypotheses that two distributions stem from
208 continuous distributions with the same medians, while the Kolmogorov-Smirnov test assumes normally distributed data
209 as null hypotheses. Probabilities of 1 denotes a consistency check while 0 indicated a value lower than 0.01.

211 Magnitude of completeness M_c is the value above which the GR relation holds, defining the complete
212 part of the dataset. M_c is a critical parameter in b -value determination, because underestimating M_c
213 leads to systematic underestimates of b -values (Woessner and Wiemer, 2005). Since catalogue
214 completeness depends on the distribution of seismic stations, which changes over time,
215 spatiotemporal variations in completeness are expected in every catalogue. Overall, completeness is
216 expected to improve over time as network density increases. Separate local assessments of M_c are
217 thus required for different periods. The steady improvement of the global seismographic network
218 raised the GCMT catalogue's completeness level from values of 5.4 and 5.5 between 1976 and 2004
219 to 5.0 after 2010 (Ekström et al., 2012). However, the M_c map (Fig. 2A) for the GCMT catalogue
220 over the entire period since 1980 shows that most M_c -values fall in the range 5.4–5.5, with only minor
221 deviations in a few particular areas along most oceanic ridges and in the Himalayan area the M_c -
222 values are slightly lower, between 5.1 and 5.3. This is probably due to an arbitrary choice of the
223 catalog authors of selecting lower cut-off minimum magnitudes for such zones.

224
225 We automatically selected different classes of cylindrical radii (from 200 to 1,500 km) to select
226 GCMT earthquakes for the maps in Figures 1 and 2. The selected radii (Fig. 2B) depended on the
227 density of local data and formed the basis for calculating M_c - and b -values. In line with the stability
228 criteria for M_c and b described in the section 2.2, the higher the number of events in the area
229 surrounding each node, the smaller the sampling radius. For GCMT, the smallest radii are assigned
230 at locations with a high density of events (red dots), i.e. subduction zones. Lower event density in
231 continental and especially ridge areas means that wider radii were needed to obtain the required
232 minimum number of events.

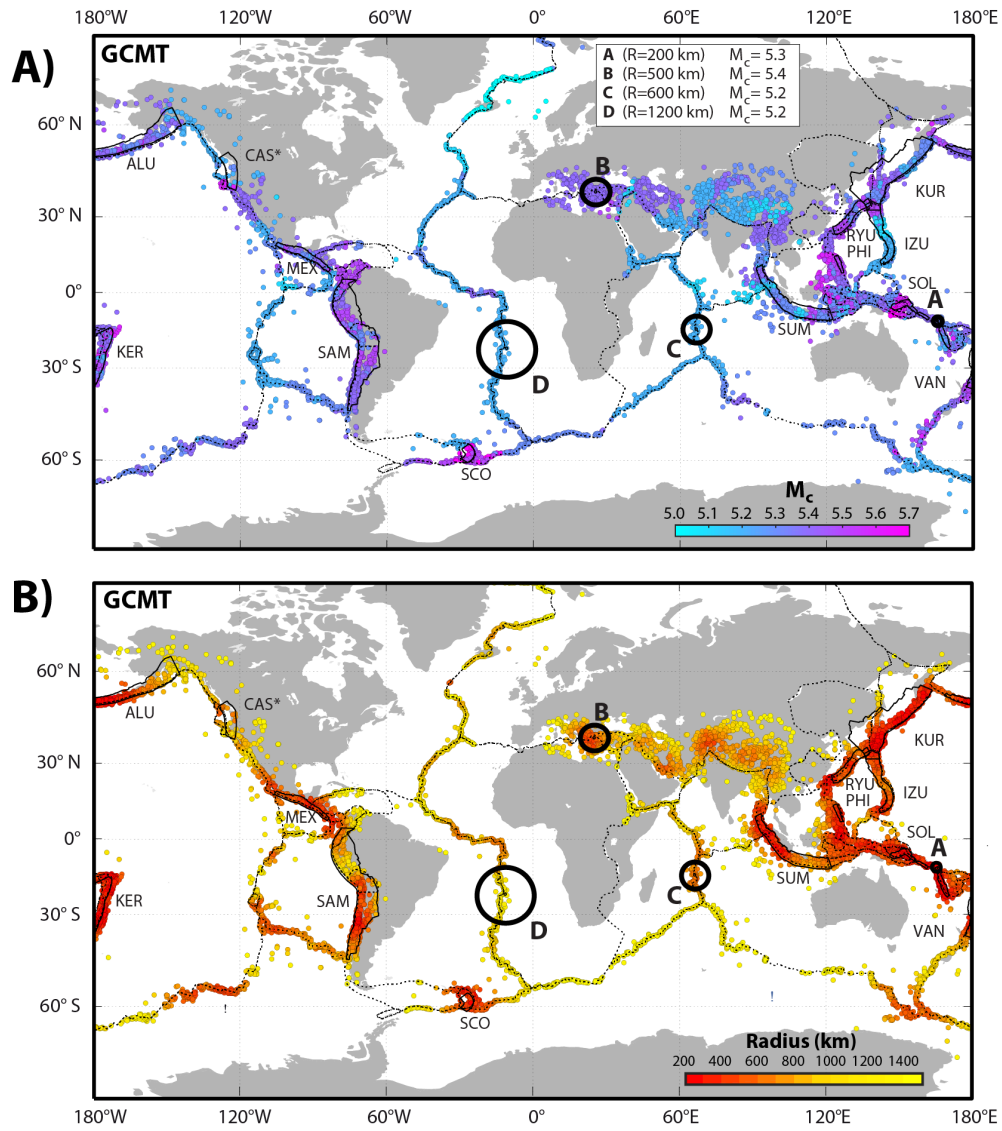


Figure 2. Global map of M_c (A) and of selection radius R (B) for the GCMT catalog (1980–2016, depth = 0 – 50 km). Points A, B, C, D, plate boundaries, subduction zones are the same as in Fig. 1.

3. Global b dependence on tectonic styles: rake and plunge angles

The focal mechanisms (FMs) can also be used to test for the influence of differential stress on b -values (Fig. 3A). This approach was first proposed by Schorlemmer et al. (2005) (hereafter referred as S2005), who demonstrated the b -value's systematic dependence on the FM's rake angle, λ . To test whether faulting style and hence differential stress systematically influences b -values, we validated the $b(\lambda)$ dependency observed by S2005 using independent data collected by global seismic networks over the past 10 years. We used the longer period now available, compared to S2005 (2004 update),

244 to reassess the systematic dependency of b -values on earthquakes' rake angle. We followed the exact
245 same procedure of S2005, barring one modification: instead of using overlapping rake bins with a
246 width, γ , of 40° (Fig. 3B, left panel), the higher number of events (12,448 compared to the original
247 7,636) allowed us to reduce this value to 20° (Fig. 3B, right panel) revealing that within a given style
248 there is a dependency on differential stress. For this analysis, we cut the whole catalogue at the overall
249 completeness magnitude of $M_c = 5.5$ and show the analysis for plane 1 and the full study period
250 (1980–2016).

251 Global seismotectonic structures are clearly reflected in the distribution of FM rake angles (Fig. 3A):
252 besides abundant plate-interface TH seismicity in subduction zones (blue, $\lambda \sim 90^\circ$), NR events
253 (green, $\lambda \sim -90^\circ$) are characteristic for ridges, shallow off-trenches and continental rifts, while SS
254 events (red, $\lambda \sim 0^\circ$, approximately 180°) occur partially along ridges and continental margins.

255 By reassessing the rake angle dependence of b , results obtained by S2005 are shown in grey and are
256 almost identical to the rake dependency obtained when data from the last 10 years is added (γ of 40° ,
257 Fig. 3B left). With $\gamma = 20^\circ$ (Fig. 3B right), instead, we find that peak b -values are offset from 'pure'
258 NR events ($\lambda = -90^\circ$) by approximately 45° . Using the Wilcoxon test, for the sake of completeness,
259 we formally tested the null hypothesis (no rake dependence for b -values) against the alternative
260 scenario hypothesized according to S2005. We compared the residual distributions (summed on all
261 λ_i) of our data ($\gamma = 40^\circ$) with respect to S2005 and 'constant b ' models, by bootstrapping 1,000 times.

262 The two histograms (see Fig. S3) differ by a level of significance smaller than 0.01, meaning that
263 there is the 99% probability that they are surely different.

264 We have also verified the same b - λ dependence for both nodal planes and different periods
265 individually (see Fig. S4). We used a depth layer of 0 to 50 km, while varying the period (1980–2004,
266 1980–2016 and 2005–2016 on different rows) and parameter γ ($\pm 20^\circ$, $\pm 30^\circ$, $\pm 40^\circ$ in different
267 columns). All frames display b -values associated with magnitude data for the nodal planes 1 and 2
268 (as indicated arbitrarily by the authors of the catalogue Ekström et al. (2012)). The chosen periods

269 were the original one S2005 (1980–2004, for which we set M_c at 5.5, indicated with a grey frame),
270 the updated one (1980–2016, where again $M_c = 5.5$) and the new, independent period (2005–2016,
271 where we set M_c at 5.2). The same “harmonic” trend, as defined by Petruccelli et al. (2018), applied
272 to all time- γ combinations. Variation in selection ranges parameter (γ) enhanced the smoothing effects
273 of b - λ trends (Schorlemmer et al., 2005). In fact, lower γ -values enable the detection of different
274 peaks relative to vertical thrust and normal mechanisms and makes each b estimations independent
275 with respect to each other (Petruccelli et al., 2018). In such view, the three Anderson regimes (NR-
276 TH-SS) would correspond to quasi-stable attractor modes ($b \sim 1.15$, $b \sim 1$ and $b = 0.9$), centered
277 around the optimal orientations (Roberts et al., 2016), with hybrid behavior resulting in a mixture of
278 such models in between, with rather rapid transitions between them.

279 We also analyzed the faulting-style dependence of b in detail by introducing an innovative b -value
280 analysis. In addition to the rake angle, three plunge angles – δ_P , δ_T , and δ_B – can also be used to infer
281 the tectonic style of a FM. Ranging from 0° to 90° , δ angles correspond to the dip (with respect to the
282 horizontal direction) of the P, B, and T axes (corresponding to moment tensor eigenvectors), with
283 sizes (eigenvalues) ranging from the lowest to the highest, respectively. Such axes form an orthogonal
284 system and, as a first approximation, permit a reasonable estimation of the principal stress directions
285 s_1 , s_2 , s_3 (Célérier, 2010). In the ternary diagram (or triangle), each corner corresponds to a 'pure'
286 tectonic style ($\delta = 90^\circ$), and each point is unequivocally defined by the three δ angles (Frohlich, 2001;
287 Frohlich and Apperson, 1992; Serpelloni et al., 2007). The original classification (Frohlich and
288 Apperson, 1992) defined strike-slip and normal mechanisms as those having δ_B and δ_P greater than
289 60° respectively, and thrust earthquakes as having δ_T greater than 50° . Mechanisms that did not satisfy
290 any of these criteria were classified as 'odd' and occupy the central part of the ternary diagram. We
291 plotted each earthquake above the overall completeness level (5.5) on the diagram and computed a
292 corresponding b -value by sampling its 500 nearest neighbor events within the diagram (Fig. 4). Since
293 events in a ternary diagram tend to cluster, we did not use samples from an equal tessellation, which

294 may have resulted in major differences in the number of selected events, but instead adopted the
295 nearest neighbor selection strategy to preserve b -value pattern continuity. Ternary diagrams result
296 extremely useful when, given a FMs distribution, a synoptic view of the seismotectonic of a certain
297 region is needed (see Fig. S2).

298 We sampled neighboring earthquakes (Fig. 4A, smoothing effects of our procedure showed in Fig.
299 S5) in a ternary diagram representation of plunge angles δ_{PTB} , allowing us not only to see rake angle
300 λ dependency (S2005), but also the full complexity of focal mechanisms (FM), including then also
301 the possible combination of two styles (mixed style). This analysis confirmed the first-order pattern
302 seen in the global survey: higher, intermediate, and lower b -values for NR (left corner), SS (top
303 corner), and TH (right corner) events respectively.

304 However, this representation revealed previously unknown systematic b -value variations along the
305 bottom edge of the ternary diagram, when transitioning from NR and TH earthquakes. The very
306 lowest b -values ($b = 0.7$) were observed for low-angle thrust faults ($50^\circ \lesssim \delta_T \lesssim 60^\circ$, $5^\circ \lesssim \beta \lesssim 15^\circ$)
307 while the highest b -values ($b = 1.4$) occur for steep normal faults ($30^\circ \lesssim \delta_T \lesssim 40^\circ$, $75^\circ \lesssim \beta \lesssim 85^\circ$).
308 Figures. 4B and 4D illustrate how the ternary diagram (Fig. 4A) and rake-based analyses of FM
309 introduced in 2005 (Fig. 3B, right) are related: the sampled rake windows of the FMs roughly span
310 triangular δ selections inside the ternary diagram, thus equally reflecting the differences in b -values
311 for NR and TH events (Fig. 4C). Note that 'pure' dip-slip faults ($\lambda = \pm 90^\circ$) are located at the bottom
312 of the triangle, whereas 'pure' strike-slips ($\lambda = 0, \pm 180^\circ$) align along the diagram's vertical altitude.

313

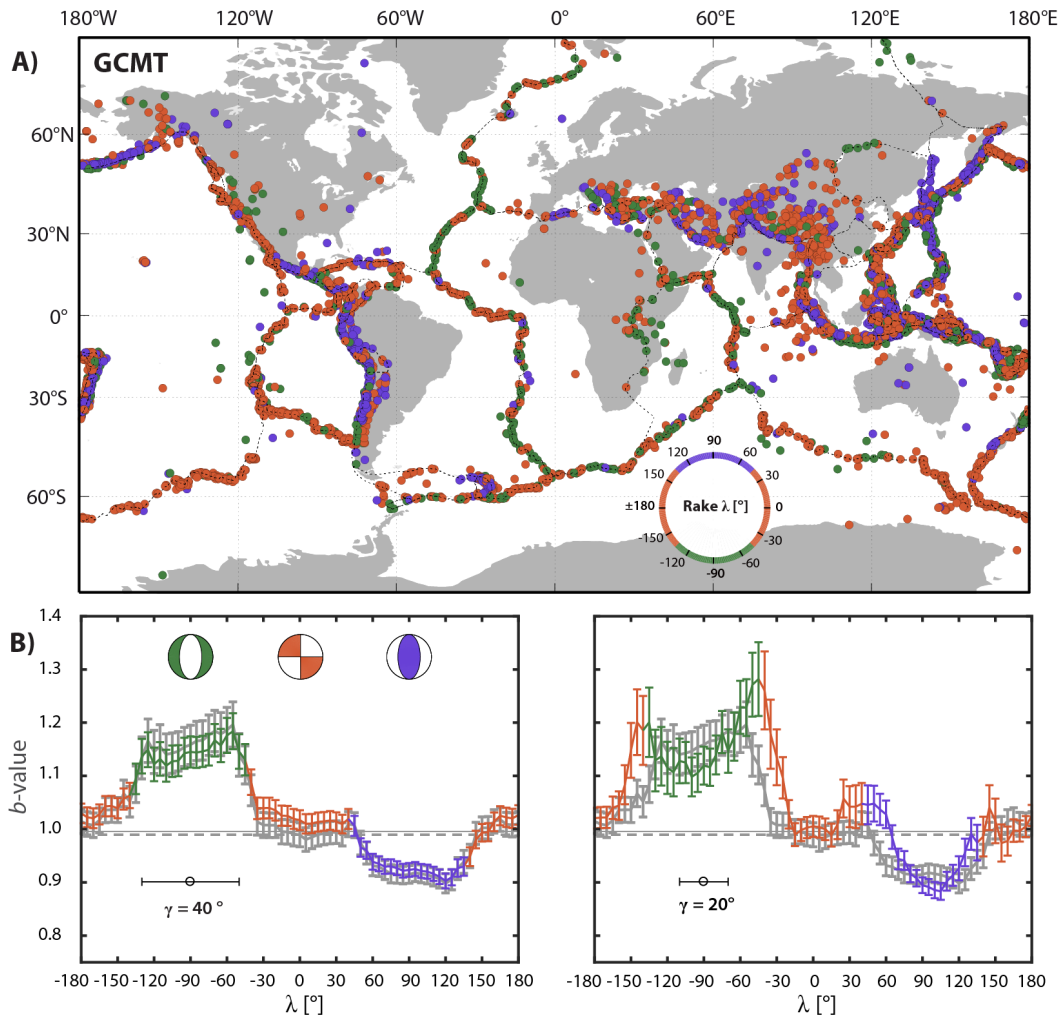


Figure 3. A) Map view of Global CMT FMs (1st nodal plane). Green: NR mechanisms, blue: TH mechanisms, red: SS mechanisms. B) Variations in b -values with rake angle λ for bin widths $\gamma = 40^\circ$ (left) and $\gamma = 20^\circ$ (right). Grey: results from S2005 (1980-2004, $z = 0-50$ km, $M_c \geq 5.5$, $\gamma = 40^\circ$). Vertical bars: Shi and Bolt uncertainties (Shi and Bolt, 1982). Horizontal grey lines: b -values for the entire S2005 datasets (dashed) and for the updated catalogue (solid).

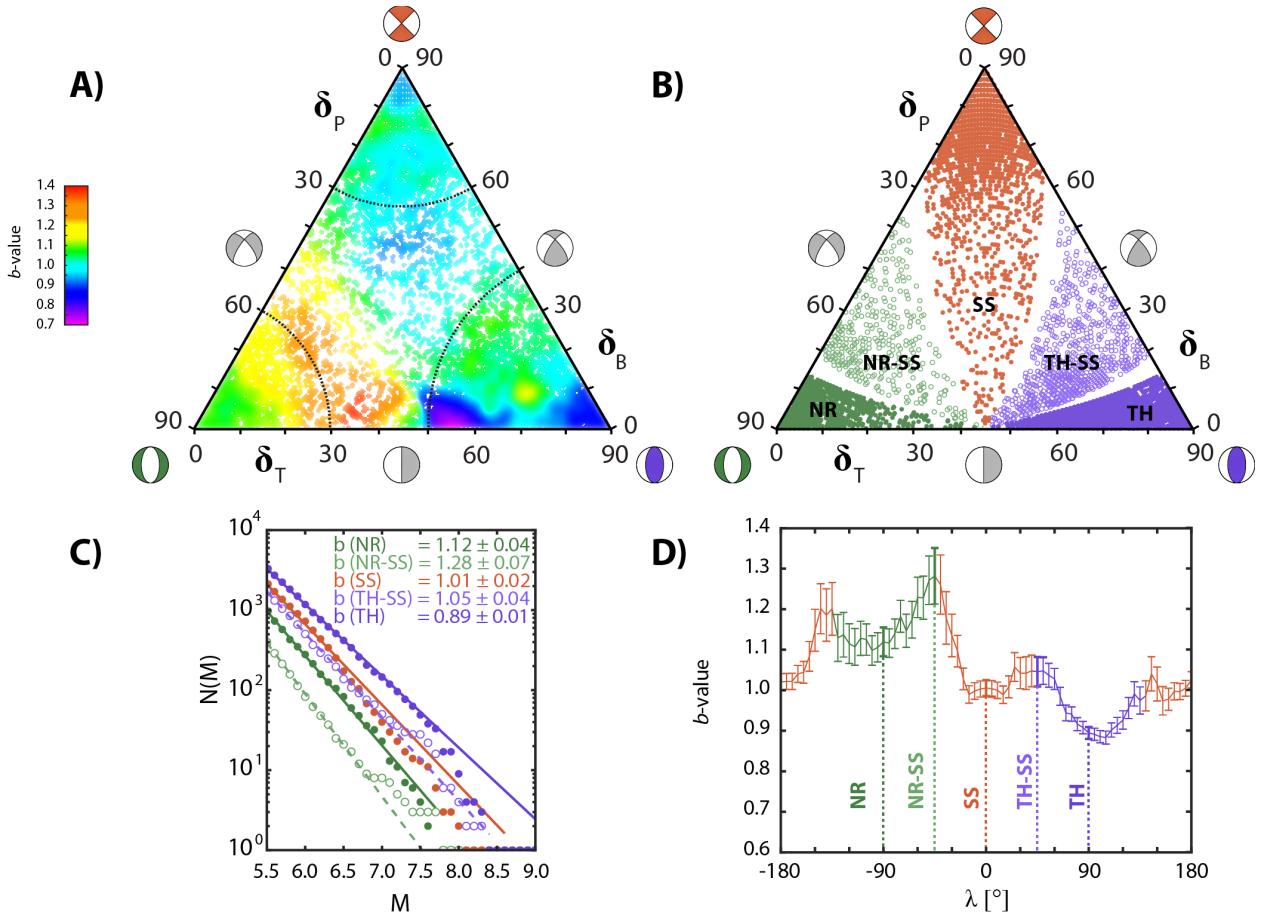


Figure 4. a) The Global CMT FM ternary-based b -values diagram. b). A) b -value mapping inside the FM triangle using the nearest neighbours approach (see MM): black dotted lines delineate areas of almost 'pure' NR, SS, and TH events. B) + D) Association between rake values (dotted vertical lines $\pm 90^\circ$, $\pm 45^\circ$, 0°) with a sampling bins of 20° (same as Fig. 3B, right panel) and representation in the ternary plot for those selected rake bins. C) Earthquake-size distributions for subsets of B: the a -value for TH-SS is doubled for plotting purposes.

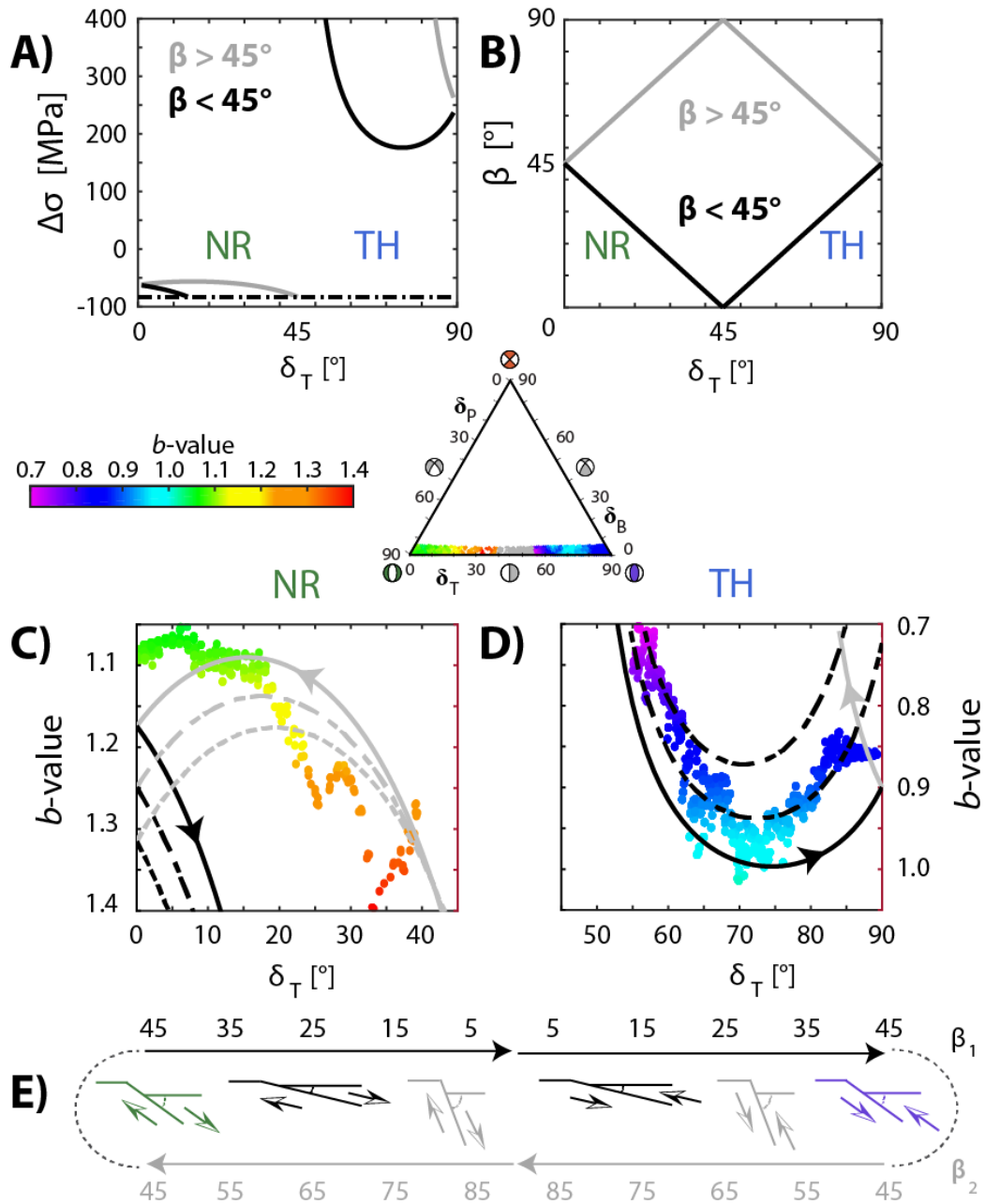
4. A unified framework to link b -values, faulting style and differential stress

In Figure 5A, we plotted the dependency of equation (2), illustrating that TH regimes are subject to higher absolute stresses than NR regimes. Moreover, this can be applied to four different cases (Fig. 5B), as the β - δ_T relationship leads to four different possibilities (see eq. A.17-18): steeply dipping (grey curves, $\beta > 45^\circ$) and shallowly dipping (black curves, $\beta < 45^\circ$) planes for the two tectonic styles (NR, with $\delta_T < 45^\circ$ and TH, with $\delta_T > 45^\circ$). In correspondence of the NR-TH corners ($\delta_T \sim 0 - 90^\circ$) both dip planes tend to 45° (Fig. 5B) but, as moving toward the center of the diagram, one solution (gray) tends to 90° while the complementary one (black) tends to 0° . In other terms, our model describes the reactivation cycle of a dip-slip fault with β (or δ_T): a high-dip NR is likely to failure with respect to a low-dip NR, as it is subjected to lower differential stress (in absolute value), resulting then in an increase of the proportion of smaller events (high b -value). Similarly, a low-dip TH is physically favorite with respect to a high-dip TH, resulting then in an increase of the proportion of big events (low b -value).

In fact, according to (4), starting from b_{FS} , TH and NR b -values suffer a decrease (-) and an increase (+) respectively, with different modulations (stronger for TH (-) and with respect to NR (+)) whose shape is governed by plunge δ_T and friction μ . Figures 5C, D then show a comparison of the analytical solutions (eq. 4, corresponding lines and regimes of Fig. 5A) as a function of δ_T or β (Fig. 5E) for NR and TH regimes respectively. Equation (4) specifically predicts the highest b -values (Fig. 5C, grey curves) for steep normal faults (Fig. 5E, left side, grey faulting scheme), and the lowest ones (Fig. 5D, black curves) for shallow thrust faults (Fig. 5E, right side, black faulting scheme), explaining the observation of the ternary analysis (Fig. 4) and confirming what anticipated above by equation (2). Note that data from $\delta_T = 40^\circ$ to $\delta_T = 55^\circ$ (grey points in the above triangle in Fig. 5) should not be considered, because purely horizontal or vertical motion cases ($\delta_T \cong 45^\circ$) represent a singularity of the problem. In fact, here the differential stresses required for fracturing would provide some unrealistic solutions, as both mechanisms become more vertical or horizontal ($\beta = 90^\circ, 0^\circ$, Fig. 5B)

353 and the requested tectonic stress $\Delta\sigma$ for faulting rises steadily (Fig. 5A). We achieve for most plunges
 354 (especially for TH regime) an excellent fit in the shape of the observed dependence and plunge and
 355 the analytical solution.

356



357

358 **Figure 5.** A) “Pure” dip-slip ($\lambda = \pm 90^\circ$) differential-stress curves (2): cohesion $C = 0$ MPa, friction $\mu = 0.6$, maximum
 359 compressive stress $\Delta\sigma = 400$ MPa. The horizontal dash-dotted line indicates a lithostatic stress of 83 MPa ($\rho = 2700$
 360 kg/m^3 , $z = 5000$ m). B) $\beta(\delta_T)$ relations: optimal planes (NR and TH corners) are expected to dip at $\beta = 45^\circ$, while, moving
 361 towards the centre of the diagram, one orientation rotates towards the vertical ($\beta = 90^\circ$) and the other towards the

horizontal ($\beta = 0^\circ$) (see text). C) NR ($\delta_B \leq 5^\circ$, $\delta_T \leq 40^\circ$, see triangle above) GCMT b -values of (4) with different μ on
plunge angles δ_T or dip angles $\beta_{1,2}$ (bottom, see E)). Parameters for equation (4): $C = 10$ MPa, friction values $\mu = 0.6$
(solid), 0.7 (dash-dotted), 0.8 (dashed). D) Same as C) but for TH ($\delta_B \leq 5^\circ$, $\delta_T \geq 55^\circ$) regime. E) Dip-slip faulting schemata
for NR and TH regimes: arrows describe reactivation processes of dip-slip faults with dip β : β_1 refers to a low-dip plane,
 β_2 to a high-dip plane.

Strike-slip faults fill the upper part of the ternary diagram with intermediate b -values (0.9 – 1.0 , Fig.
4), in agreement with the intermediate differential stress levels predicted equations (3) and (4).
However, while for dip-slip fault zones we can rely on the fact that one of the principal stress is
vertical (or almost vertical), for strike-slip faults it is not possible to establish a direct, unequivocal
link between the strike of the slip vector (which determines the amount of differential stress for a SS)
and the plunges (C  lerier, 2010). We therefore cannot derive a unique equation relating differential
stress and faulting style for primarily strike-slip earthquakes.

374

375 5. Conclusions

We developed a unifying, empirical framework that links Anderson’s faulting theory and differential
stress with the earthquake-size distribution. Our analytical solution (eq. 4 and Fig. 5) tally closely
with globally observed b -values, and explain both first-order observations (Petrucelli et al., 2018)
and also second-order variations our approach revealed: our theory predicts that contrary to previous
assumptions (S2005) the lowest b -values should not be observed for ‘pure’ TH events with a 45° dip,
but should rather occur for very shallowly dipping TH events (Figs. 4A, 5D), such as Chilean
subduction zones (Fig. S2B). Likewise, our model predicts that the highest b -values should occur for
NR to SS regimes, not for ‘pure’ NR events (Figs. 4A, 5C).

Overall, we find it remarkable how systematically b -values vary with faulting style (Figs. 4, 5) and
with tectonic region (Figs. 1, 2). Even more remarkable to us is the fact that a simple geo-mechanical
formulation based solely on Anderson’s faulting theory from 1905 and the Mohr-Coulomb failure

387 criterion, which dates back to 1776, can explain empirical observations. We established this
388 framework based on global data, because their broadest range of tectonic provinces and FM diversity
389 covered with a homogeneous dataset. However, the underlying principles are universal and should
390 apply to earthquakes at all scales. One of the first implications of our research is thus that we offer
391 regional and local-scale applications a quantitative framework to linking earthquake-size distribution
392 and tectonic regimes. The model we derived can and should now be tested using independent data,
393 either using regional, high-quality earthquake catalogues or in lab-based studies linking stress and
394 the faulting styles of acoustic emissions. We also suggest that the ternary diagram analysis introduced
395 in Figure 4 constitutes a powerful new way to study b -values and their relationship to faulting at all
396 scales.

397 The analysis of b -values and faulting mechanisms is prone to many uncertainties in data, such as
398 location and magnitude uncertainties or systematic biases (Kagan, 1999; 2010), and faulting styles
399 and tectonic regimes are sometimes poorly known and highly heterogeneous. These complexities,
400 improvements in earthquake processing and the fact that we have developed for this study more
401 sophisticated analysis techniques may explain why the first order observations we present here have
402 taken until today to be discovered.

403 The theory supporting inverse linearity between b -value and differential stress gain an important
404 contribution with this work. We validate results obtained in the controlled and reproducible
405 conditions of rock laboratories (Amitrano, 2003) for acoustic emissions of magnitudes -4 and ruptures
406 of micro-meters, until the largest earthquakes of magnitude 5.5 and higher.

407 Equally important is our test of the rake dependency of b -value against independent data collected in
408 the past 13 years (Fig. 3) that establishes with very high confidence that global b -value vary
409 statistically significantly (Fig. S2) with rake also in a fully prospective test setting.

410 The b -value is used in all studies of seismic hazard as a tool to relate the more frequent small event
411 with the infrequent larger ones. It is possibly the most critical parameter in all seismogenic source

412 models. We suggest that the overwhelming evidence of the b -value depending on differential stress
413 and tectonic style demands a shift in the way seismic hazard assessment (SHA) is conducted at local,
414 regional and global scale. Essentially all SHA studies conducted to date and most earthquake forecast
415 models use only empirical observations of b -values for the region, because, so far, no theory was
416 available to link it with geological properties. We believe that our results not only open up a pathway
417 for a much deeper, geologically inspired interpretation of observed spatially varying b -value; they
418 also allow to build different kinds of seismogenic source models that combine knowledge on
419 tectonics, observed faulting styles and past observed earthquakes into one self-consistent model. This
420 will be especially important for regions with low to moderate seismicity, where empirical data offer
421 poor constraints on the frequency of the largest events.

422

423 **Appendix A**

424 **Dip-slip fault modelling**

425 According to Anderson's theory, (as an absolute value) the applied shear stress $\Delta\tau$ for dip-slip faults
426 is:

$$427 \quad |\Delta\tau| = \frac{1}{2}\Delta\sigma \sin 2\theta \quad (\text{A.1})$$

428 where $\Delta\sigma$ is the tectonic stress and the angle θ is the complementary angle to the dip angle $\beta = \pi/2 -$
429 θ . With respect to β , this results in:

$$430 \quad |\Delta\tau| = \frac{1}{2}\Delta\sigma \sin 2\theta = \frac{1}{2}\Delta\sigma \sin[\pi - 2\beta] = \frac{1}{2}\Delta\sigma \sin 2\beta \quad (\text{A.2})$$

431 We express Anderson's faulting criterion for dip-slip faults in terms of δ_T along the bottom of the
432 ternary diagram (Figs. 4, 5). The plunge angle δ_T is linked to the vertical component of the T-axis
433 vector t_z (Gasperini and Vannucci, 2003)

$$434 \quad \delta_T = \arcsin t_z \quad (\text{A.3})$$

435 that can be computed by calculating the sum of the vertical components of the outward normal n_z and
436 of the slip vector d_z

$$437 \quad t_z = \frac{n_z + d_z}{\sqrt{2}} \quad (\text{A.4})$$

438 Such vectors are a function of both the dip angle and the rake angle

$$439 \quad n_z = -\cos \beta \quad (\text{A.5})$$

$$440 \quad d_z = -\sin \beta \sin \lambda \quad (\text{A.6})$$

441 Accordingly, the plunge angle δ_T , as a function of both the dip and rake angles, is

$$442 \quad \delta_T = \arcsin \left[\frac{-\cos \beta - \sin \beta \sin \lambda}{\sqrt{2}} \right] \quad (\text{A.7})$$

443 Along the bottom line connecting the NR vertex and the TH vertex, the rake angle is $\lambda = \pm 90^\circ$
 444 (C  lerier, 2010), so

$$445 \quad \delta_T = \arcsin \left[\frac{-\cos \beta \mp \sin \beta}{\sqrt{2}} \right] = \arcsin \left[-\frac{\cos \beta \pm \sin \beta}{\sqrt{2}} \right] \quad (\text{A.8})$$

446 where the plus sign (+) applies to TH and the minus sign (-) applies to NR faulting. Equation (A.8)
 447 can be rewritten as

$$448 \quad \sqrt{2} \sin \delta_T = \begin{cases} -\cos \beta + \sin \beta & NR \\ -\cos \beta - \sin \beta & TH \end{cases} \quad (\text{A.9})$$

449 The linear combination, or harmonic addition, of sine and cosine waves is equivalent to a single sine
 450 wave with a phase term φ and an amplitude factor A

$$451 \quad a_1 \sin \alpha + a_2 \cos \alpha = A \sin(\alpha + \varphi) \quad (\text{A.10})$$

452 where the original amplitudes a_1 and a_2 summed in quadrature provide A

$$453 \quad A = \sqrt{a_1^2 + a_2^2} \quad (\text{A.11})$$

454 while

$$455 \quad \varphi = \text{atan} \left(\frac{a_2}{a_1} \right) \quad (\text{A.12})$$

456 Thus, TH provides two solutions for β as a function of δ_T (remembering that $\sin \alpha = \sin(\pi - \alpha)$)

$$457 \quad \sqrt{2} \sin \delta_T = \sqrt{2} \sin(\beta + 45^\circ) \Rightarrow \beta = \delta_T - 45^\circ \quad (\text{A.13})$$

$$458 \quad \sqrt{2} \sin \delta_T = \sqrt{2} \sin[180^\circ - (\beta + 45^\circ)] = \sqrt{2} \sin(135^\circ - \beta) \Rightarrow \beta = 135^\circ - \delta_T \quad (\text{A.14})$$

459 Similarly, for the NR regime the phase terms are -45° and 135°

$$460 \quad \sqrt{2} \sin \delta_T = \sqrt{2} \sin(\beta - 45^\circ) \Rightarrow \beta = \delta_T + 45^\circ \quad (\text{A.15})$$

$$461 \quad \sqrt{2} \sin \delta_T = \sqrt{2} \sin(\beta + 135^\circ) = \sqrt{2} \sin[180^\circ - (45^\circ - \beta)] = \sqrt{2} \sin(45^\circ - \beta) \Rightarrow \beta = 45^\circ - \delta_T \quad (\text{A.16})$$

462 The 4 solutions (A.13-16) for β (two dip angles for two nodal planes and two tectonic styles), which
 463 describe how to switch from plunge δ_T to β (and vice versa) through linear relations, are displayed in
 464 Figure 5B and can be summarized as:

$$465 \quad NR(0^\circ \leq \delta T \leq 45^\circ) \beta(\delta_T) = \begin{cases} 45^\circ - \delta_T \\ 45^\circ + \delta_T \end{cases} \quad (A.17)$$

$$466 \quad TH(45^\circ \leq \delta T \leq 90^\circ) \beta(\delta_T) = \begin{cases} \delta_T - 45^\circ \\ 135^\circ - \delta_T \end{cases} \quad (A.18)$$

467 So, 'pure' NR and TH dip at 45° while, moving toward the center, the dip of one plane increases to
 468 90° while the other decreases to 0° .

469 We can assume that the vertical stress σ_z is always lithostatic pressure, whereas horizontal stress σ_y
 470 varies according to tectonic stress (assuming that stresses are positive for TH and negative for NR):

$$471 \quad \sigma_z = \rho g z \quad (A.19)$$

$$472 \quad \sigma_y = \rho g z + \Delta \sigma \quad (A.20)$$

473 Since, in this instance, vertical and horizontal stress also equal the maximum and minimum principal
 474 stress, tectonic and differential stress are the same (i.e. $\Delta \sigma = \sigma_1 - \sigma_3$).

475 Assuming this configuration (Fig. S5), deriving the normal and shear stress along the fault zone is
 476 quite a straightforward calculation. We consider a dip-slip fault dipping at an angle β ranging from
 477 (0° to 90°) (vertical directed downward). The components of the outward normal versor n are then

$$478 \quad \hat{n} = \begin{pmatrix} -\sin \varphi \sin \beta \\ \cos \varphi \sin \beta \\ -\cos \beta \end{pmatrix} \quad (A.21)$$

479 where angle φ is the strike direction. Since differential stress for dip-slip configurations does not
 480 depend on strike direction (see main text) unlike the strike-slip case, we are allowed to set $\varphi = 0^\circ$ for
 481 the sake of simplicity.

482 Then, the traction components T_i write as

$$T_i = \sigma_{ij}n_j = (\sigma_x \quad \sigma_y \quad \sigma_z) \begin{pmatrix} 0 \\ \sin \beta \\ -\cos \beta \end{pmatrix} = \begin{pmatrix} 0 \\ \sigma_y \sin \beta \\ -\sigma_z \cos \beta \end{pmatrix} \quad (\text{A.22})$$

The scalar product of the traction and the normal provides the normal stress σ_n

$$\sigma_n = \vec{T} \cdot \hat{n} = \sigma_y \sin^2 \beta + \sigma_z \cos^2 \beta = \sigma_y \frac{1-\cos 2\beta}{2} + \sigma_z \frac{1+\cos 2\beta}{2} = \frac{\sigma_z + \sigma_y}{2} + \frac{\sigma_z - \sigma_y}{2} \cos 2\beta \quad (\text{A.23})$$

where we have used the duplication formulas for sine and cosine. We assume that the shear stress vector τ is oriented as the slip vector d (see Fig. S5)

$$\vec{\tau} = \begin{pmatrix} \sin \lambda \cos \beta \sin \psi + \cos \lambda \cos \psi \\ -\sin \lambda \cos \beta \cos \psi + \cos \lambda \sin \psi \\ -\sin \beta \sin \lambda \end{pmatrix} = \begin{pmatrix} \cos \lambda \\ -\sin \lambda \cos \beta \\ -\sin \beta \sin \lambda \end{pmatrix} \quad (\text{A.24})$$

Then, the shear stress comes from the scalar product of the traction with shear stress vector

$$\tau = \vec{\tau} \cdot \hat{n} = -\sigma_y \sin \lambda \sin \beta \cos \beta + \sigma_z \sin \lambda \sin \beta \cos \beta = \frac{1}{2} \sin 2\beta \sin \lambda (\sigma_z - \sigma_y) \quad (\text{A.25})$$

where we have used the multiplication formula for the sine. For “pure” dip-slip mechanisms ($\lambda = \pm 90^\circ$, lower part of the triangle, upper sign for TH, lower sign for NR), (S25) becomes

$$\tau = \pm \frac{1}{2} \sin 2\beta (\sigma_z - \sigma_y) \quad (\text{A.26})$$

By using the expression of the stress in (A.19-20)

$$\sigma_n = \rho g z + \frac{\Delta \sigma}{2} (1 - \cos 2\beta) \quad (\text{A.27})$$

$$\tau = \mp \frac{\Delta \sigma}{2} \sin 2\beta \quad (\text{A.28})$$

assuming positive stresses for TH ($\Delta \sigma > 0$) and negative stresses for NR ($\Delta \sigma < 0$).

Using a Mohr-Coulomb criterion (Coulomb, 1776) defined as:

$$|\tau| = C + \mu(\sigma_n - p) \quad (\text{A.29})$$

where C is cohesion, μ is the frictional coefficient (between 0.6 and 1 for most rocks (Turcotte, D. L., & Schubert, 2002)) and p is pore pressure (considered here as hydrostatic, and used for completeness).

502 Substituting the values for σ_n and τ as a function of $\Delta\sigma$ gives us:

503 $|\tau| = \left| \mp \frac{\Delta\sigma}{2} \sin 2\beta \right| = \pm \frac{\Delta\sigma}{2} \sin 2\beta$ (A.30)

504 with the plus sign (+) for TH ($\Delta\sigma > 0$) and the minus sign (-) for NR ($\Delta\sigma < 0$). Then:

505 $\pm \frac{\Delta\sigma}{2} \sin 2\beta = C + \mu(\rho g z - p) + \mu \frac{\Delta\sigma}{2} (1 - \cos 2\beta)$ (A.31)

506 Finally, solving for $\Delta\sigma$ gives us the equation (2):

507
$$\Delta\sigma = \frac{C + 2\mu(\rho g z - p)}{\pm \sin 2\beta - \mu(1 - \cos 2\beta)}$$
 (A.32)

508 If we assume a lithostatic stress of 83 MPa (with a density of 2,700 kg/m³ and a depth of 5,000 m
509 with hydrostatic pressure), a friction coefficient in the range 0.6-0.8, and a cohesionless fault (i.e. C
510 = 0 MPa), we obtain the plot shown in Figure 5A.

511 Equation (A.32) admits real values if

512 $\pm \sin 2\beta - \mu(1 - \cos 2\beta) \neq 0$ (A.33)

513 This can be rewritten as

514 $\pm \sin 2\beta + \mu \cos 2\beta \neq \mu$ (A.34)

515 According to harmonic addition, the left term in A.28 can be separated in (remembering that the
516 tangent has a period of 180°)

517 $\sqrt{1 + \mu^2} \sin[\pm 2\beta + \text{atan } \mu] \neq \mu$ (A.35)

518 $\sqrt{1 + \mu^2} \sin[\pm 2\beta + \text{atan } \mu - \pi] \neq \mu$ (A.36)

519 But remember that $\sin(\text{atan } \mu) = \mu / \sqrt{1 + \mu^2}$

520 $\begin{cases} \sin[\pm 2\beta + \text{atan } \mu] \neq \sin[\text{atan } \mu] \\ \sin[\pm 2\beta + \text{atan } \mu - \pi] \neq \sin[\text{atan } \mu] \end{cases} \Rightarrow \begin{cases} \beta \neq 0^\circ \\ \beta \neq 90^\circ \end{cases}$ (A.37)

521 for both tectonic styles. Using (A.17-A.18), these values correspond to $\delta_T = 45^\circ$ which thus represents
522 a singularity of the problem.

523 **Strike-slip fault modelling**

524 As already reported in the manuscript, dip-slip modeling is feasible because in this configuration at
525 least one of principal axes is assumed to be vertical. For other zones of the ternary diagram,
526 unfortunately, this cannot be done, because univocal relationships do not exist (see Celerier, 2010).
527 The center of the diagram represents a mixture of different styles, while the inclined edges rely on
528 different hypotheses for the stress states (NR-SS and TH-SS), as explained above.

529

530 For example, for strike-slip (top of the triangle), for which both σ_1 and σ_3 lies on the horizontal plane,
531 the differential stress depends on a different angle (strike), say ψ (Anderson, 1905), not on dip β
532 anymore (close to 90°),

$$533 \Delta\sigma_{SS} = \frac{2\mu(\rho gz - p)}{\pm \sin 2\psi + \mu \cos(2\psi)} \quad (A.38)$$

534 Using the Anderson theory of faulting, faulting starts ($\frac{d}{d\psi} [\Delta\sigma_{SS}] = 0$) as soon as condition

$$535 \cot \psi = \pm \mu$$

536 is satisfied (see Turcotte and Schubert 2002, equation 8.36). Considering sign conventions (ψ
537 positive in top quadrants and negative in bottom quadrants), just for “pure” pure-strike-slip ($\lambda=0$,
538 $\pm 180^\circ$), we came out with a total of 8 possible expressions for linking a plunge (δ_B in this case) and
539 ψ (four quadrants and two possible slip directions, positive and negative). Moreover, it is impossible
540 to distinguish in ternary diagram from left-lateral mechanisms to right lateral mechanisms, as they
541 inevitably fall in the same region (central-top part of the diagram) (see also Celerier, 2010).

To summarize, the differential stress necessary to reactivate a strike-slip fault would not be related to how much the fault can dip (as happens for a dip-slip fault) but instead would depend along which (horizontal) directions the fault might slip, if a strike angle (with respect to σ_1 , for instance, ranging from $-\pi$ to π) is defined. The reactivation process of a strike-slip fault does not establish a direct, univocal link between the strike of the slip vector (which determines the amount of differential stress for a SS) and the plunges of B axis (for which b -values are known, from Fig. 3), differently from dip-slip case where relations for the fault dip and the plunges of T axis are possible. Therefore, the limit for the SS case is represented by the metric of the ternary space, since its usage implies that the position of each event in the diagram has to depend on plunge angles, which are in turn related to the vertical components of the moment tensor principal axes, as well as the impossibility in knowing the real directions of stress principal axes.

GR b -value goodness-of-fit-test

According to GR model (Aki, 1965), the cumulative number of earthquakes detected at each binned magnitude M is

$$N(M) = 10^{a-bM} \quad (\text{A.39})$$

For each frequency-magnitude distribution, then, by setting the maximum magnitude of the model as equal to the maximum magnitude detected, percentages of fit can be estimated as

$$p_{FIT} = 1 - \frac{\sum |M_i - m_i|}{\sum M_i} \quad (\text{A.40})$$

(where M and m are the empirical and the theoretical magnitudes).

565 **References**

- 566 Aki, K., 1965. Maximum Likelihood Estimate of b in the Formula $\log N = a - bM$ and its Confidence Limits. *Earthq. Res.*
 567 Institute, Univ. Tokyo.
- 568 Amitrano, D., 2012. Variability in the power-law distributions of rupture events. *Eur. Phys. J. Spec. Top.* 205, 199–215.
 569 <https://doi.org/10.1140/epjst/e2012-01571-9>
- 570 Amitrano, D., 2003. Brittle-ductile transition and associated seismicity: Experimental and numerical studies and
 571 relationship with the b value. *J. Geophys. Res.* 108, 1–15. <https://doi.org/10.1029/2001JB000680>
- 572 Anderson, E.M., 1905. The dynamics of faulting. *Trans. Edinburgh Geol. Soc.* 8, 387–402.
 573 <https://doi.org/10.1144/transed.8.3.387>
- 574 Bird, P., 2003. An updated digital model of plate boundaries. *Geochemistry, Geophys. Geosystems* 4.
 575 <https://doi.org/10.1029/2001GC000252>
- 576 Boettcher, M.S., Jordan, T.H., 2004. Earthquake scaling relations for mid-ocean ridge transform faults. *J. Geophys. Res.*
 577 *B Solid Earth.* <https://doi.org/10.1029/2004JB003110>
- 578 Cao, A., Gao, S.S., 2002. Temporal variation of seismic b -values beneath northeastern Japan island arc. *Geophys. Res.*
 579 *Lett.* 29, 43–48. <https://doi.org/10.1029/2001GL013775>
- 580 Célérrier, B., 2010. Remarks on the relationship between the tectonic regime, the rake of the slip vectors, the dip of the
 581 nodal planes, and the plunges of the P , B , and T axes of earthquake focal mechanisms. *Tectonophysics* 482, 42–
 582 49. <https://doi.org/10.1016/j.tecto.2009.03.006>
- 583 Coulomb, C.A., 1776. Essai sur une application des regles des maximis et minimis a quelques problemes de statique
 584 relatifs, a la architecture. *Mem. Acad. Roy. Div. Sav.* 7, 343–387.
- 585 Ekström, G., Nettles, M., Dziewoński, A.M., 2012. The global CMT project 2004-2010: Centroid-moment tensors for
 586 13,017 earthquakes. *Phys. Earth Planet. Inter.* 200–201, 1–9. <https://doi.org/10.1016/j.pepi.2012.04.002>
- 587 Farrell, J., Husen, S., Smith, R.B., 2009. Earthquake swarm and b -value characterization of the Yellowstone volcano-
 588 tectonic system. *J. Volcanol. Geotherm. Res.* 188, 260–276. <https://doi.org/10.1016/j.jvolgeores.2009.08.008>
- 589 Frohlich, C., 2001. Display and quantitative assessment of distributions of earthquake focal mechanisms. *Geophys. J.*

590 Int. 144, 300–308. <https://doi.org/10.1046/j.1365-246X.2001.00341.x>

591 Frohlich, C., Apperson, K.D., 1992. Earthquake focal mechanisms, moment tensors, and the consistency of seismic
592 activity near plate boundaries. *Tectonics* 11, 279–296. <https://doi.org/10.1029/91TC02888>

593 Gasperini, P., Vannucci, G., 2003. FPSPACK: A package of FORTRAN subroutines to manage earthquake focal
594 mechanism data. *Comput. Geosci.* 29, 893–901. [https://doi.org/10.1016/S0098-3004\(03\)00096-7](https://doi.org/10.1016/S0098-3004(03)00096-7)

595 Ghosh, A., Newman, A. V., Thomas, A.M., Farmer, G.T., 2008. Interface locking along the subduction megathrust
596 from b-value mapping near Nicoya Peninsula, Costa Rica. *Geophys. Res. Lett.* 35.
597 <https://doi.org/10.1029/2007GL031617>

598 Goebel, T.H.W., Schorlemmer, D., Becker, T.W., Dresen, G., Sammis, C.G., 2013. Acoustic emissions document stress
599 changes over many seismic cycles in stick-slip experiments. *Geophys. Res. Lett.* 40, 2049–2054.
600 <https://doi.org/10.1002/grl.50507>

601 Gulia, L., Wiemer, S., 2010. The influence of tectonic regimes on the earthquake size distribution: A case study for
602 Italy. *Geophys. Res. Lett.* 37. <https://doi.org/10.1029/2010GL043066>

603 Gutenberg, B., Richter, C.F., 1944. Frequency of earthquakes in California. *Bull. Seismol. Soc. Am.* 34, 185–188.

604 Hayes, G.P., Wald, D.J., Johnson, R.L., 2012. Slab1.0: A three-dimensional model of global subduction zone
605 geometries. *J. Geophys. Res. Solid Earth* 117. <https://doi.org/10.1029/2011JB008524>

606 Kagan, Y.Y., 2010. Earthquake size distribution: Power-law with exponent $\beta \equiv 1/2$? *Tectonophysics* 490, 103–114.
607 <https://doi.org/10.1016/j.tecto.2010.04.034>

608 Kagan, Y.Y., 1999. Universality of the Seismic Moment-frequency Relation. *Pure Appl. Geophys.* 155, 537–573.
609 <https://doi.org/10.1007/s000240050277>

610 Kagan, Y.Y., 1997. Seismic moment-frequency relation for shallow earthquakes: Regional comparison. *J. Geophys.*
611 *Res.* 102, 2835. <https://doi.org/10.1029/96JB03386>

612 MOGI, K., 1962. Study of elastic shocks caused by the fracture of heterogeneous materials and its relation to
613 earthquake phenomena. *Bull. Earthq. Res. Inst., Univ. Tokyo* 40, 125–173.

614 Nishikawa, T., Ide, S., 2014. Earthquake size distribution in subduction zones linked to slab buoyancy. *Nat. Geosci.* 7,
615 904–908. <https://doi.org/10.1038/ngeo2279>

616 Okal, E.A., Romanowicz, B.A., 1994. On the variation of b-values with earthquake size. *Phys. Earth Planet. Inter.* 87,

55–76. [https://doi.org/10.1016/0031-9201\(94\)90021-3](https://doi.org/10.1016/0031-9201(94)90021-3)

Petrucelli, A., Vannucci, G., Lolli, B., Gasperini, P., 2018. Harmonic Fluctuation of the Slope of the Frequency–
Magnitude Distribution (b-Value) as a Function of the Angle of Rake. *Bull. Seismol. Soc. Am.*
<https://doi.org/10.1785/0120170328>

Roberts, N.S., Bell, A.F., Main, I.G., 2016. Mode switching in volcanic seismicity: El Hierro 2011–2013. *Geophys. Res. Lett.* 43, 4288–4296. <https://doi.org/10.1002/2016GL068809>

Roberts, N.S., Bell, A.F., Main, I.G., 2015. Are volcanic seismic b-values high, and if so when? *J. Volcanol. Geotherm. Res.* <https://doi.org/10.1016/j.jvolgeores.2015.10.021>

Sammonds, P.R., Meredith, P.G., Main, I.G., 1992. Role of pore fluids in the generation of seismic precursors to shear fracture. *Nature* 359, 228–230. <https://doi.org/10.1038/359228a0>

Samowitz, I.R., Forsyth, D.W., 1981. Double seismic zone beneath the Mariana Island Arc. *J. Geophys. Res. Solid Earth* 86, 7013–7021. <https://doi.org/10.1029/JB086iB08p07013>

Scholz C. H., 2002. *The Mechanics of Earthquakes and Faulting*, 2nd Editio. ed. Cambridge University Press.

Scholz, C.H., 2015. On the stress dependence of the earthquake b value. *Geophys. Res. Lett.* 42, 1399–1402. <https://doi.org/10.1002/2014GL062863>

Scholz, C.H., 1968. The frequency-magnitude relation of microfracturing in rock and its relation to earthquakes. *Bull. Seismol. Soc. Am.* 58, 399–415.

Schorlemmer, D., Wiemer, S., 2005. Earth science: Microseismicity data forecast rupture area. *Nature* 434, 1086–1086. <https://doi.org/10.1038/4341086a>

Schorlemmer, D., Wiemer, S., Wyss, M., 2005. Variations in earthquake-size distribution across different stress regimes. *Nature* 437, 539–542. <https://doi.org/10.1038/nature04094>

Schorlemmer, D., Wiemer, S., Wyss, M., 2004. Earthquake statistics at Parkfield: 1. Stationarity of b values. *J. Geophys. Res. B Solid Earth* 109, 1–17. <https://doi.org/10.1029/2004JB003234>

Serpelloni, E., Vannucci, G., Pondrelli, S., Argnani, A., Casula, G., Anzidei, M., Baldi, P., Gasperini, P., 2007. Kinematics of the Western Africa-Eurasia plate boundary from focal mechanisms and GPS data. *Geophys. J. Int.* 169, 1180–1200. <https://doi.org/10.1111/j.1365-246X.2007.03367.x>

Shi, Y., Bolt, B., 1982. The standart error of the magnitude-frequency b-value. *Bull. Seismol. Soc. Am.* 72, 1677–1687.

644 Spada, M., Tormann, T., Wiemer, S., Enescu, B., 2013. Generic dependence of the frequency-size distribution of
645 earthquakes on depth and its relation to the strength profile of the crust. *Geophys. Res. Lett.* 40, 709–714.
646 <https://doi.org/10.1029/2012GL054198>

647 Stein, S., Okal, E.A., 2007. Ultralong period seismic study of the December 2004 Indian Ocean earthquake and
648 implications for regional tectonics and the subduction process. *Bull. Seismol. Soc. Am.* 97.
649 <https://doi.org/10.1785/0120050617>

650 Stern, R.J., Fouch, M.J., Klemperer, S.L., 2003. An overview of the Izu-Bonin-Mariana subduction factory. *Insid.*
651 *Subduction Fact.* 138, 175–222. <https://doi.org/10.1029/138GM10>

652 Tormann, T., Enescu, B., Woessner, J., Wiemer, S., 2015. Randomness of megathrust earthquakes implied by rapid
653 stress recovery after the Japan earthquake. *Nat. Geosci.* 8, 152–158. <https://doi.org/10.1038/ngeo2343>

654 Tormann, T., Wiemer, S., Hardebeck, J.L., 2012. Earthquake recurrence models fail when earthquakes fail to reset the
655 stress field. *Geophys. Res. Lett.* 39. <https://doi.org/10.1029/2012GL052913>

656 Tormann, T., Wiemer, S., Mignan, A., 2014. Systematic survey of high-resolution b value imaging along Californian
657 faults: Inference on asperities. *J. Geophys. Res. Solid Earth.* <https://doi.org/10.1002/2013JB010867>

658 Turcotte, D. L., & Schubert, G., 2002. *Geodynamics*, 2nd Editio. ed. Cambridge University Press.

659 Utsu, T., 1966. A Statistical Significance Test of the Difference in b-value between Two Earthquake Groups. *J. Phys.*
660 *Earth* 14, 37–40. <https://doi.org/10.4294/jpe1952.14.37>

661 Uyeda, S., 1982. Subduction zones: An introduction to comparative subductology. *Tectonophysics* 81, 133–159.
662 [https://doi.org/10.1016/0040-1951\(82\)90126-3](https://doi.org/10.1016/0040-1951(82)90126-3)

663 Uyeda, S., Kanamori, H., 1979. Back-arc opening and the mode of subduction. *J. Geophys. Res.* 84, 1049.
664 <https://doi.org/10.1029/JB084iB03p01049>

665 Wiemer, S., Wyss, M., 2002. Mapping spatial variability of the frequency-magnitude distribution of earthquakes. *Adv.*
666 *Geophys.* 45. [https://doi.org/10.1016/S0065-2687\(02\)80007-3](https://doi.org/10.1016/S0065-2687(02)80007-3)

667 Wiemer, S., Wyss, M., 2000. Minimum magnitude of completeness in earthquake catalogs: Examples from Alaska, the
668 Western United States, and Japan. *Bull. Seismol. Soc. Am.* 90, 859–869. <https://doi.org/10.1785/0119990114>

669 Woessner, J., Wiemer, S., 2005. Assessing the quality of earthquake catalogues: Estimating the magnitude of
670 completeness and its uncertainty. *Bull. Seismol. Soc. Am.* 95, 684–698. <https://doi.org/10.1785/0120040007>

671 Yang, W., Hauksson, E., Shearer, P.M., 2012. Computing a large refined catalog of focal mechanisms for southern
672 California (1981-2010): Temporal stability of the style of faulting. *Bull. Seismol. Soc. Am.* 102, 1179–1194.
673 <https://doi.org/10.1785/0120110311>

674

675

676 **Supplementary Material**

677 **Zoom into main seismotectonic structures**

678 The Mariana subduction zone (Fig. S2A) is part of a convergent oceanic margin roughly 2,800 km in
679 length. Here, the old seafloor is subducting deep into the crust, giving rise to widespread volcanic
680 activity and hydrothermal emissions and a high level of very deep earthquake activity compared to
681 other subduction zones (Stern et al., 2003). As the ternary diagram (Fig. S2A) shows, both
682 compression and extension can coexist in such zones. Indeed, downdip tension in the lower zone and
683 down-dip compression in the upper zone have been previously described (Samowitz and Forsyth,
684 1981): thermal stresses and inelastic unbending of the upper part of the slab cause low-magnitude
685 shallow seismicity, consistent with generally high b -values.

686 The Chilean subduction zone (Fig. S2B) originates from the subduction of the Nazca Plate beneath
687 the South America Plate and is associated with widespread and relatively high-magnitude TH
688 seismicity, including the largest ever observed earthquake, with a magnitude of $M = 9.6$. In this
689 regime, strong coupling between the overriding plates probably causes very high differential stresses,
690 so low b -values are observed. The offshore spreading ridge and fracture zone to the south
691 (characterised by NR and SS seismicity) exhibit distinctly higher b -values.

692 Seismicity along the spreading rifts and transform faults of mid-oceanic ridges (Fig. S2C) has
693 previously been associated with higher b -values than the global average (Kagan, 1997). Given these
694 systems' low coupling coefficient, the bulk of deformation along them occurs aseismically. While
695 spreading ridges are characterised by volcanic activity and associated NR seismicity, transform faults
696 generate numerous slow earthquakes, their length and linearity triggering rather small, strike-slip

697 earthquakes (Boettcher and Jordan, 2004). High pore pressures and the extensional regime suggest
698 low differential stresses in these regions, which are consistently reflected by high measured b -values.
699 Continental collision zones are typified by strong tectonic heterogeneity on spatial scales that exceed
700 the resolution capabilities of this global study. Thus, here we cannot distinguish between individual
701 local regimes and their imprints on local b -values. Instead, we observe overall intermediate b -values
702 for continental collision boundaries, partially with a tendency towards lower b -values e.g. in the
703 Himalayan region (e.g., Fig. S2D), but we also note a tendency towards higher b -values in the
704 European area. Continental rift systems like the East African Rift are characterised by high b -values,
705 as expected in an extensional regime.

706

707

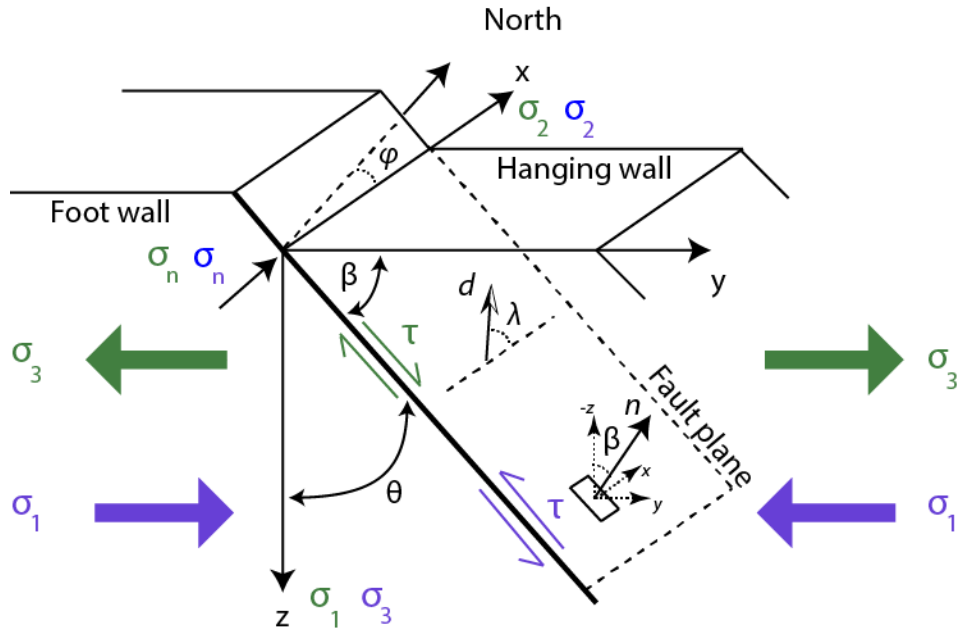
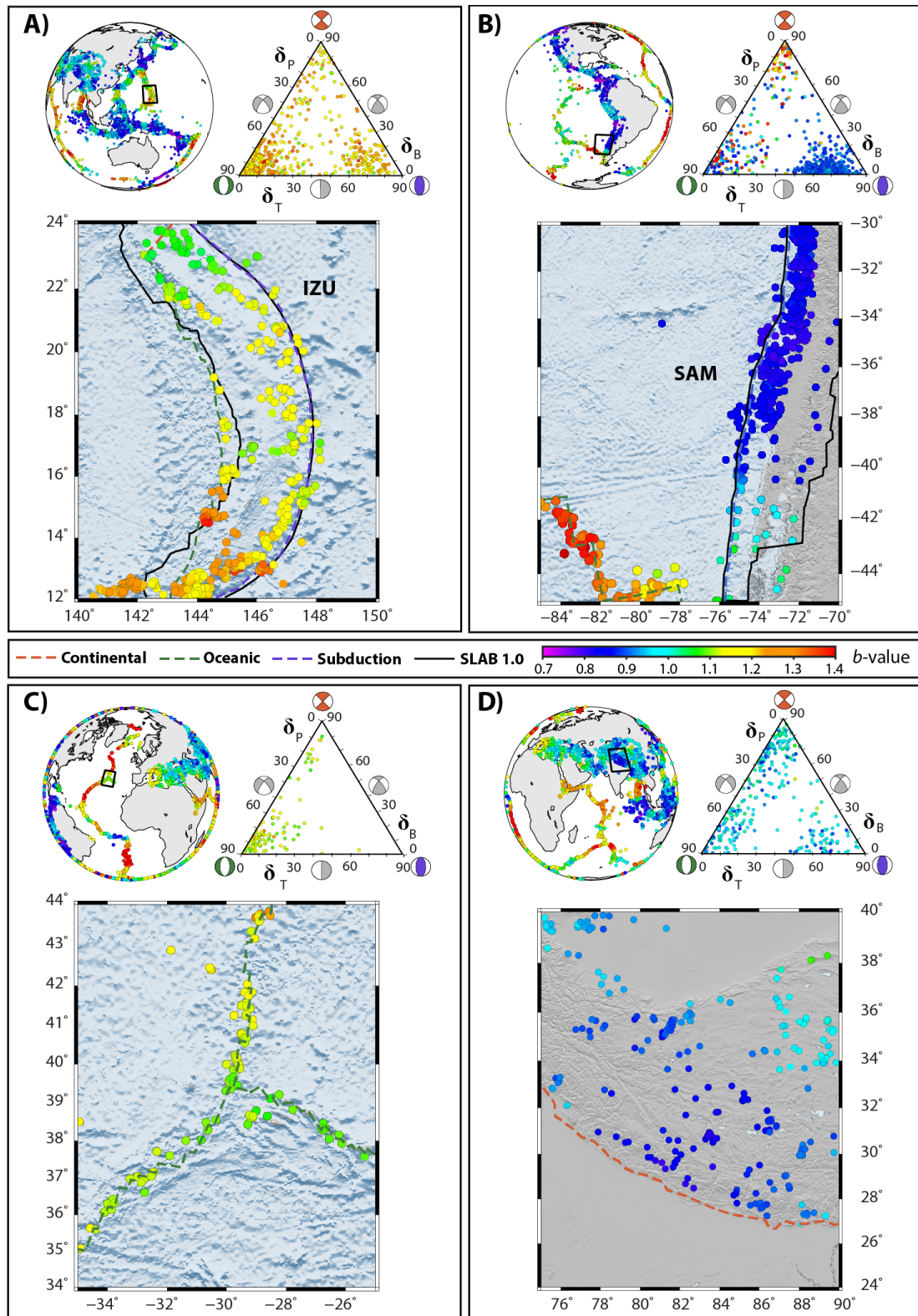


Figure S1. Dip-slip faulting schemes and principal axes orientations (see Appendix A). If one principal stress (σ_1 or σ_3) is always assumed to be along the vertical z and the intermediate one σ_2 lies on one horizontal directions y , the dip-slip faulting mechanisms (NR - green - and TH - blue) are easily inferred and the tectonic stress $\Delta\sigma_{HV}$ acting on the fault is the differential stress $\Delta\sigma = \sigma_1 - \sigma_3$. Vectors: σ_n = normal stress, τ = shear stress, n = fault plane normal, d = slip vector. Angles: β = fault dip angle, ϕ = fault strike angle (set to 0° in our model), λ = rake angle, θ = complementary of β .



715

716

717

718

719

720

Figure S2. Detailed views of different seismotectonic structures, illustrating b -values in a map view (from Fig. 1A) and ternary diagrams. A) Mariana subduction zone: mostly NR and TH events, all with high b -values. B) Chilean subduction zone: most TH events display low b -values (high b -value SS and NR events occur along oceanic ridge faults in the southwest). C) Oceanic ridge: mostly NR, some SS events with high and very high b -values. D) Continental collision zone (Himalaya): mixture of event types with intermediate b -values.

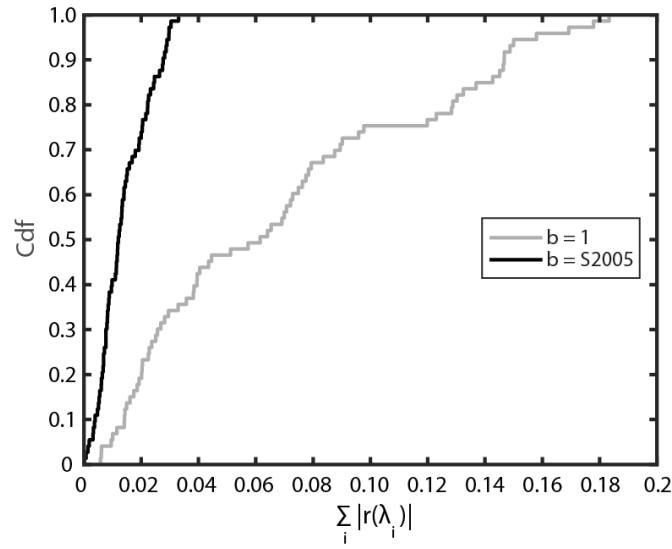


Figure S3. Empirical cumulative density functions (Cdf) for the sum residuals of the Figure 4B ($\gamma=40^\circ$) data with respect to a constant $b=1$ model (gray) and to S2005 (black) data. The two curves are significantly different at 0.01.

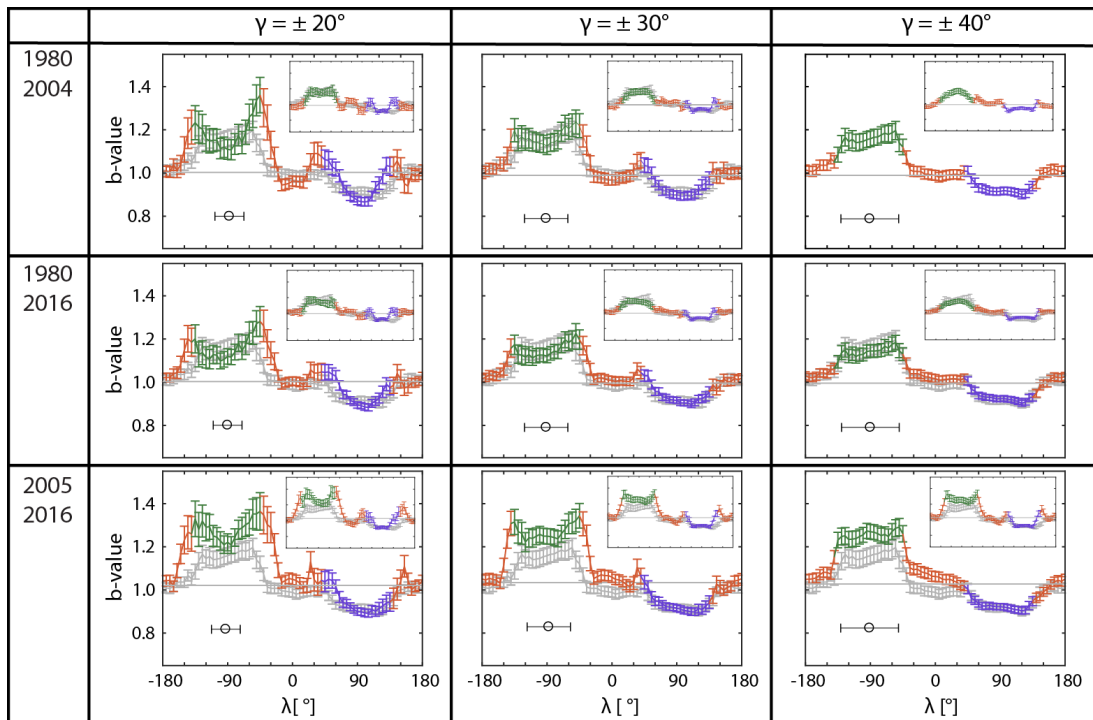


Figure S4. Frames of the b -value dependence on rake angle λ for different time- γ selections (1980–2016, $\gamma = \pm 20^\circ, \pm 30^\circ, \pm 40^\circ$, common of depth = 0–50 km). Rows show different periods while columns refer to different γ value (showed as a horizontal black errorbar centered at $\lambda = -90^\circ$). Gray b - λ dependence from the original (1980–2004, $\gamma = \pm 40^\circ$) is in the background. Horizontal gray line refers to mean b -value for the specific time- γ subset. Inset upper panels are the analyses for the second nodal plane.

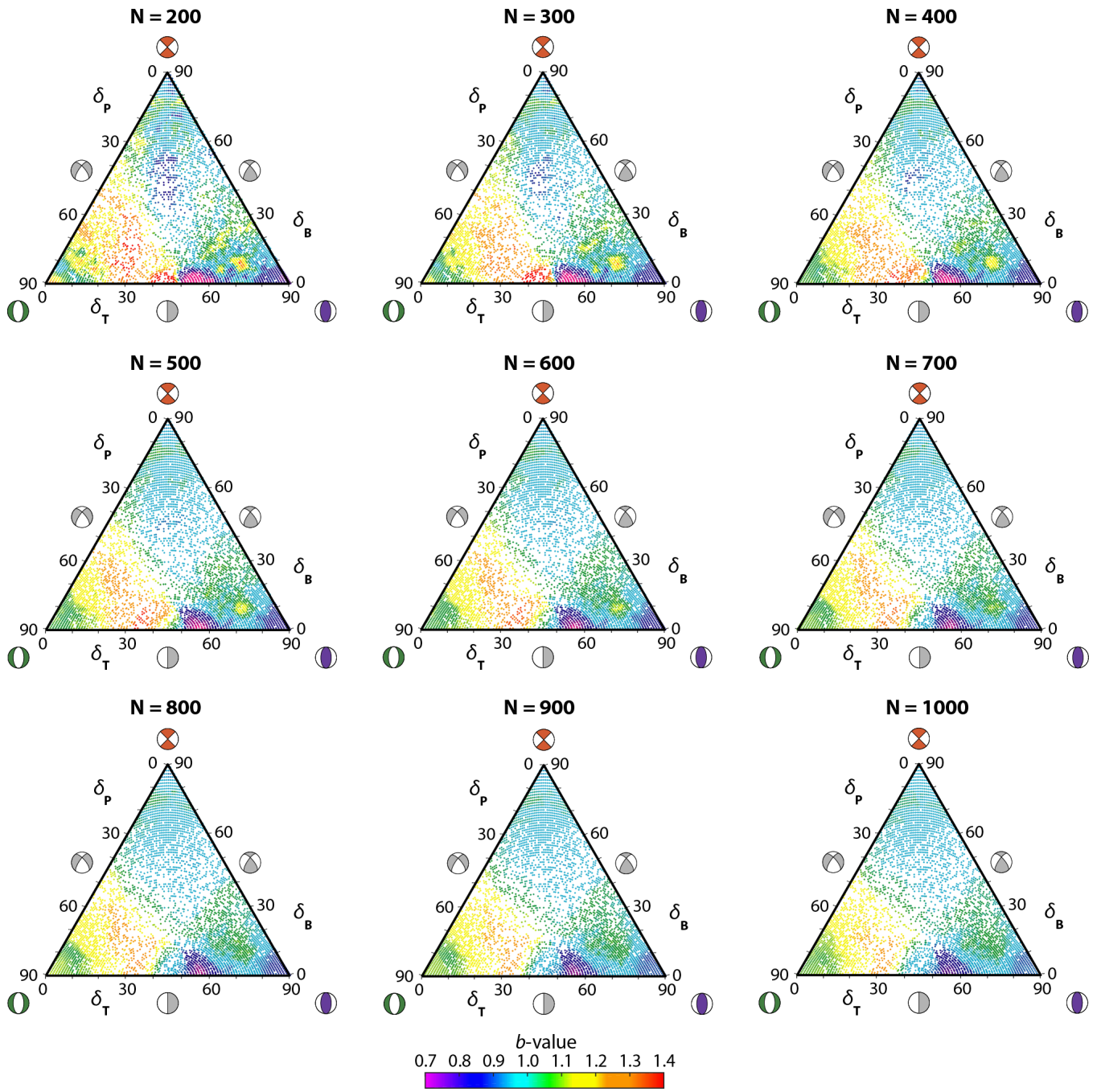


Figure S5. Ternary b -value mapping with different number of neighbors N (from 200 to 1000).